Journal of Crystal Growth 310 (2008) 4102–4109

Contents lists available at ScienceDirect

Journal of Crystal Growth

journal homepage: www.elsevier.com/locate/jcrysgro

Characterization of microstructure and defects in epitaxial ZnO $(1\,1\,\bar{2}\,0)$ films on Al_2O_3 $(1\,\bar{1}\,0\,2)$ substrates by transmission electron microscopy

Jae Wook Lee [a], Seok Kyu Han [b], Soon-Ku Hong [b,*], Jeong Yong Lee [a], Takafumi Yao [c]

[a] Department of Materials Science and Engineering, KAIST, Daejeon 305-701, Republic of Korea
[b] Department of Advanced Materials Engineering, Chungnam National University, Daejeon 305-764, Republic of Korea
[c] Center for Interdisciplinary Research, Tohoku University, Sendai 980-8578, Japan

ARTICLE INFO

Article history:
Received 30 April 2008
Received in revised form
5 June 2008
Accepted 17 June 2008
Communicated by H. Asahi
Available online 22 June 2008

PACS:
68.37.Lp
78.66.Hf
61.72.Ff
61.72.Nn

Keywords:
A1. Characterization
A1. Defects
A3. Molecular beam epitaxy
B1. Zinc compounds
B2. Semiconducting II–VI materials

ABSTRACT

Microstructure and defects in nonpolar ZnO $(1\,1\,\bar{2}\,0)$ films with different thicknesses were studied by transmission electron microscopy. The ZnO films were grown on Al_2O_3 $(1\,\bar{1}\,0\,2)$ substrates by plasma-assisted molecular beam epitaxy. The misfit dislocations were observed at the interface with regularly spaced configurations, which were well agreed with the equilibrium spacing of the misfit dislocations calculated based on the lattice misfits. The diagonal defect along the ZnO $[1\,0\,\bar{1}\,0]$ and $[0\,1\,\bar{1}\,0]$ directions and the misfit dislocations were mainly observed in the 30 nm-thick ZnO film. As increasing the film thickness, the diagonal defect was seldom observed and the threading dislocations (in addition to the misfit dislocations) were being the major defects. The dislocation densities of the 240 nm-thick ZnO film were determined to be $\sim 7.3\times10^{10}\,cm^{-2}$ for the dislocations with $\langle 0\,0\,0\,1\rangle$ Burgers vector and $\sim 6.1\times10^{9}\,cm^{-2}$ for the $\frac{1}{3}\langle 1\,1\,\bar{2}\,0\rangle$ Burgers vector, resulting in the total dislocation density of $\sim 7.9\times10^{10}\,cm^{-2}$. In addition to the perfect threading dislocations, stacking faults on $(0\,0\,0\,1)$ planes were observed. The type of stacking fault was determined to be a type-I_1 intrinsic stacking fault having the stacking sequence of (AB'ABC'BC), which has the Frank partial dislocations with the Burgers vector of $\frac{1}{6}[0\,2\,\bar{2}\,3]$ at the end. The stacking fault density of the 240 nm-thick ZnO film was determined to be $\sim 1.2\times10^{5}\,cm^{-1}$.

1. Introduction

Since the II–VI compound semiconductor ZnO has a direct wide band gap energy (3.37 eV at room temperature) and a high-exciton binding energy of 60 meV [1], it has received considerable attentions for promising applications to light-emitting devices with wavelengths ranging from blue to ultraviolet. For this purposes, most of ZnO films have been grown on Al_2O_3 $(0\,0\,0\,1)$ substrates, where the grown ZnO films have a growth direction of $\langle 0\,0\,0\,1\rangle$. In this case, a strong built-in electrostatic field appears in the ZnO film as a result of spontaneous and piezoelectric polarizations caused by the noncentrosymmetric nature of wurtzite crystal structure. The polarization-induced electric field results in the quantum confined Stark effect (QCSE) [2,3], which acts as a negative factor on a performance of the light-emitting devices [4–6]. One of the direct ways to eliminate the effect of polarization fields on devices is growing the films with nonpolar directions. Actually, growth of $(1\,0\,\bar{1}\,0)$ *M*-plane ZnO on $(1\,0\,\bar{1}\,0)$ *M*-plane sapphire substrate by metal organic vapor phase epitaxy (MOVPE) [7,8] and $(1\,0\,\bar{2}\,0)$ *A*-plane ZnO on $(1\,\bar{1}\,0\,2)$ *R*-plane sapphire substrate by molecular beam epitaxy (MBE) [9,10] were reported.

A few studies have been performed on nonpolar GaN [11,12] and ZnO films [13,14]. However, comprehensive and systematic studies on microstructural investigations of ZnO $(1\,1\,\bar{2}\,0)$ films on Al_2O_3 $(1\,\bar{1}\,0\,2)$ substrates by transmission electron microscopy (TEM) are not yet reported. Especially, investigation on threading dislocations in ZnO$(1\,1\,\bar{2}\,0)$/$Al_2O_3$$(1\,\bar{1}\,0\,2)$ is not reported.

In this article, we report detailed microstructural investigations by TEM observations along three different directions of $\langle 0\,0\,0\,1\rangle$, $\langle \bar{1}\,1\,0\,0\rangle$, and $\langle 1\,1\,\bar{2}\,0\rangle$ for the epitaxial ZnO $(1\,1\,\bar{2}\,0)$ films grown on Al_2O_3 $(1\,\bar{1}\,0\,2)$ substrates by plasma-assisted molecular-beam epitaxy (PAMBE). Especially, characteristics of the defects in epitaxial ZnO films with different film thickness are investigated and many kinds of structural defects such as misfit dislocations, diagonal defects, threading dislocations, and stacking faults are discussed based on the results obtained by two-beam diffraction contrast imaging and high-resolution (HR) phase contrast imaging techniques.

* Corresponding author. Tel.: +82 42 821 6640; fax: +82 42 822 3206.
E-mail address: soonku@cnu.ac.kr (S.-K. Hong).

0022-0248/$ - see front matter © 2008 Elsevier B.V. All rights reserved.
doi:10.1016/j.jcrysgro.2008.06.042

2. Experimental procedure

ZnO films were grown on (1 $\bar{1}$ 0 2) *R*-plane Al_2O_3 substrates by PAMBE. The substrates were degreased by ultrasonic cleaning in acetone (for 10 min) and methanol (for 10 min) at room temperature followed by rinsing with deionized (DI) water. Then the substrates were chemically etched in a solution of H_2SO_4: $H_3PO_4 = 3{:}1$ (vol%) at 160 °C for 15 min. Finally, the substrates were washed with DI water and dried by nitrogen blowing before being put into the MBE chamber.

Prior to the film growth, the substrates were thermally cleaned by heating at 700 °C in the preparation chamber for 60 min followed by a further cleaning at 800 °C in the growth chamber for 30 min under ultrahigh vacuum of 2×10^{-10} Torr achieved by a liquid nitrogen supply. Elemental Zn (6N) and oxygen radio frequency (RF) plasma were used as group II and group VI sources, respectively. All the ZnO films were grown at 700 °C. During the ZnO films growth, Zn flux was set to 2 Å/s and the oxygen flow rate was maintained at 2 sccm with an RF power of 300 W. Growth rate of the ZnO film is 3 nm/min and film thicknesses of the investigated samples are 30, 90, 180, and 240 nm.

TEM specimens were prepared by mechanical polishing with a tripod polisher followed by Ar^+ ion milling for the electron transparency. TEM observations were made from three different directions; ZnO $\langle 0\,0\,0\,1 \rangle$ and ZnO $\langle \bar{1}\,1\,0\,0 \rangle$ zone axes (cross-sectional views), and ZnO $\langle 1\,1\,\bar{2}\,0 \rangle$ zone axis (plan-view) by using a JEOL JEM 3010 electron microscope operated at 300 kV.

3. Results and discussion

Fig. 1(a) shows a cross-sectional TEM bright field (BF) micrograph and its corresponding selected area electron diffraction (SAED) pattern of the 30 nm-thick ZnO film taken along the ZnO $\langle 0\,0\,0\,1 \rangle$ zone axis. From the SAED pattern, the epitaxial relationship between ZnO film and Al_2O_3 substrate was found to be $(1\,1\,\bar{2}\,0)$ZnO//$(1\,\bar{1}\,0\,2)Al_2O_3$ and [0 0 0 1]ZnO//[$\bar{1}$ 1 0 1]Al_2O_3. We can see several defect contrasts in Fig. 1. First, we can see the strain contrast caused by misfit dislocations at the interface. Second, many diagonal lines along the ZnO [1 0 $\bar{1}$ 0] and [0 1 $\bar{1}$ 0] directions were observed in the film. These diagonal contrasts were not threading dislocations as will be shown in HR TEM (HRTEM) micrograph of Fig. 2. The observation of similar diagonal contrast has been reported in the $(1\,1\,\bar{2}\,0)$ZnO/$(1\,\bar{1}\,0\,2)LiTaO_3$ system [14].

It is surprising that the observed major defects in the film were not threading dislocations but some diagonal contrasts, instead. Fig. 1(b) and (c) shows the cross-sectional TEM BF micrographs taken at the same region of Fig. 1(a) with the diffraction vector $\mathbf{g} = 1\,1\,\bar{2}\,0_{ZnO}$ and $1\,\bar{1}\,0\,0_{ZnO}$, respectively.

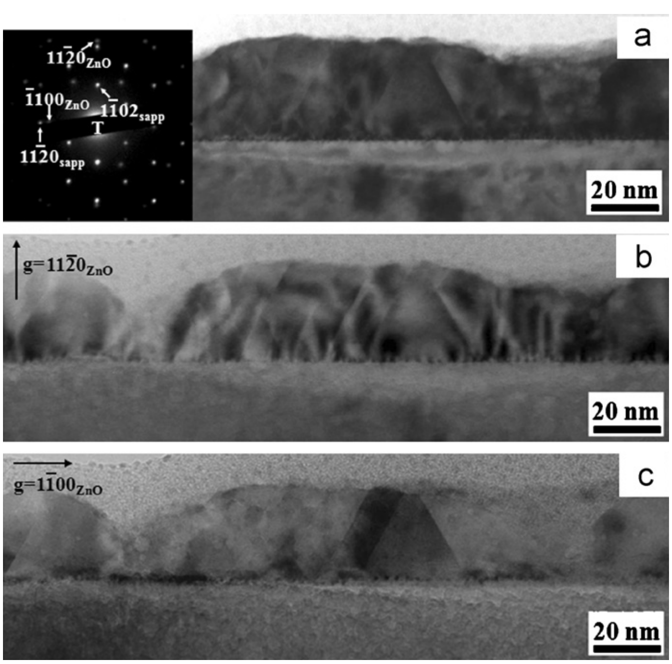

Fig. 1. Cross-sectional TEM micrographs of the 30 nm-thick ZnO film on Al_2O_3 (1 $\bar{1}$ 0 2) substrate taken near the ZnO [0 0 0 1] zone axis. (a) Zone axis BF micrograph, (b) $\mathbf{g} = 1\,1\,\bar{2}\,0_{ZnO}$ two-beam BF micrograph, and (c) $\mathbf{g} = 1\,\bar{1}\,0\,0_{ZnO}$ two-beam BF micrograph. The diagonal contrast in the film and strain contrast of misfit dislocations at the interface are clearly observed.

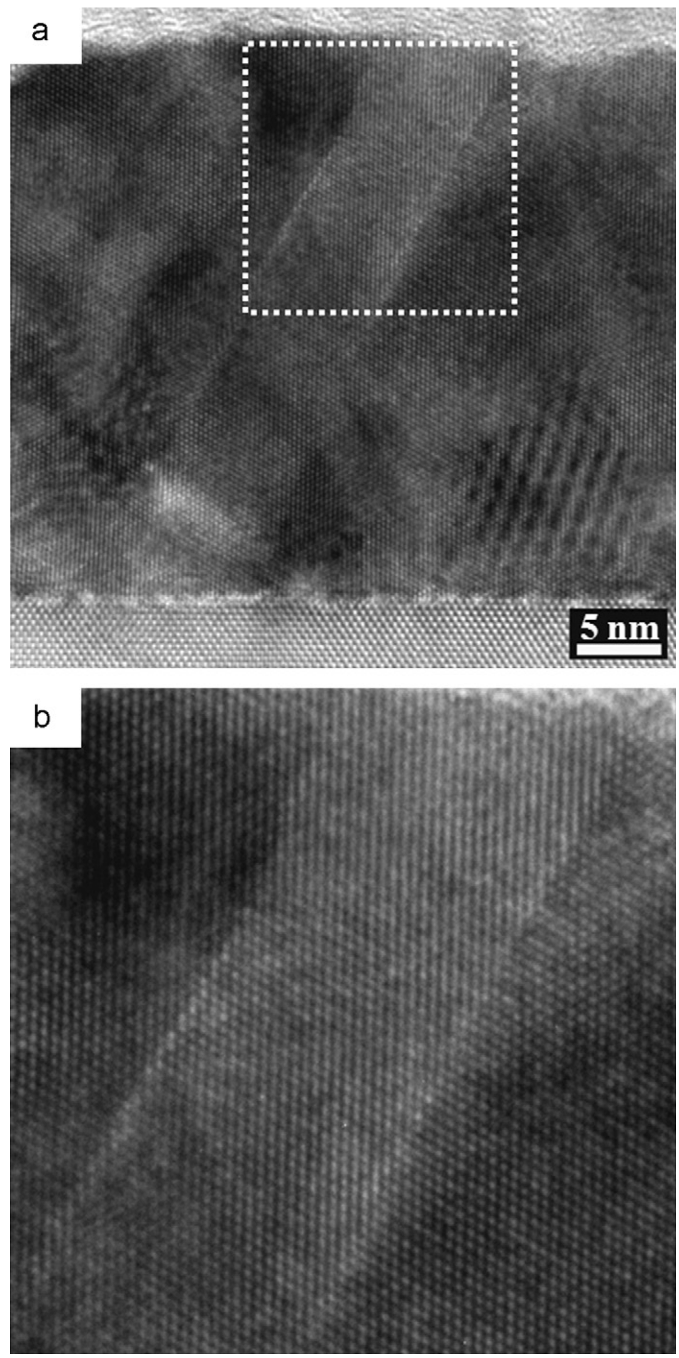

Fig. 2. (a) HRTEM micrograph for the diagonal contrast and (b) enlarged micrograph of the marked square region in (a).

Under the $\mathbf{g} = 1\,1\,\bar{2}\,0_{ZnO}$ two-beam condition, the diagonal contrast was more clearly observed. The similar contrast was reported from the $(1\,1\,\bar{2}\,0)$ZnO/$(1\,\bar{1}\,0\,2)$$LiTaO_3$ case [14]. Lim et al. [14] believed that the diagonal contrast was resulted from the displacement of ZnO atomic position from its bulk position in forming the atomic bonding with the atoms of Al_2O_3 substrate at the interface. However, finding the displacement was difficult in our samples and we cannot make a conclusion on the origin of diagonal defect in this study. Fig. 2 shows HRTEM micrographs of the diagonal contrast. We can easily recognize that the lattice images at the diagonal contrast is abnormal but we cannot see any strict and significant displacement of atoms or missing as the cases for the dislocations, stacking faults, twins, or grain boundaries.

The diagonal contrasts shown in Fig. 1 make a 60° angle with respect to the sapphire substrate. Similar inclined defects were reported in *a*-plane GaN grown on $(1\,1\,\bar{2}\,0)$ 4H-SiC prepared by organometallic vapor phase epitaxy (OMVPE) [15]. Zakharov et al. [15] explained these defects as prismatic stacking faults (PSFs). They showed a zigzag-like structure in the HR image and each of their boundaries acted as a termination or nucleation site for a basal stacking fault. However, the diagonal contrasts shown in our ZnO sample did not show the characteristics of PSFs. Namely, the contrasts in our sample were imaged as thin lines as shown in the HR image of Fig. 2 and did not show the band area of PSFs in the plan-view image under $\mathbf{g} = 1\,\bar{1}\,0\,0_{ZnO}$ condition. So, we think the diagonal contrasts shown in our ZnO film are not the PSFs.

Here, it should be noted that misfit dislocations were clearly observed at the interface as shown in Fig. 1. Considering the common fact that threading dislocations are concomitantly generated with misfit dislocations in the growth of lattice mismatched epitaxial thin films [16], the observed findings of clear observations of many misfit dislocations and the diagonal defects in the 30 nm-thick ZnO film but very seldom observation of threading dislocations is interesting. As will be discussed later, on the other hand, the diagonal defects were seldom observed as increasing the film thickness. Instead, the threading dislocations were mainly observed, which indicates that the diagonal defects did roles of strain relaxation in addition to the misfit dislocations.

Fig. 3(a) is a cross-sectional TEM BF micrograph and its corresponding SAED pattern of the same sample in Fig. 1, but the observation is taken from the ZnO $[\bar{1}\,1\,0\,0]$ zone axis. Fig. 3(b) and (c) shows the cross-sectional TEM BF micrographs taken at the same region of Fig. 3(a) with the diffraction vector $\mathbf{g} = 1\,1\,\bar{2}\,0_{ZnO}$ and $0\,0\,0\,2_{ZnO}$, respectively. Unlike the micrographs shown in Fig. 1, we could not observe the diagonal contrast in these micrographs even with the diffraction vector $\mathbf{g} = 1\,1\,\bar{2}\,0_{ZnO}$. Since the TEM micrograph is the two-dimensional projection of three-dimensional objects, the diagonal contrast along the ZnO $[1\,0\,\bar{1}\,0]$ and $[0\,1\,\bar{1}\,0]$ directions was projected perpendicular to the paper in the observation with the ZnO $[\bar{1}\,1\,0\,0]$ zone axis, which make those invisible. This means the diagonal contrast or defect has a characteristic of a planar defect as can be guessed from the HRTEM micrographs shown in Fig. 2. In addition, the strain contrast from the misfit dislocations was seldom observed in Fig. 2. But, this is because the lattice misfit along this direction is quite small as will be discussed in Fig. 4.

HRTEM micrographs of the ZnO/Al_2O_3 interface for the 30 nm-thick-sample are shown in Fig. 4. The interface was observed to be atomically sharp and semicoherent. The zone axes of Fig. 4(a) and (c) are ZnO $\langle 0\,0\,0\,1 \rangle$ and ZnO $\langle \bar{1}\,1\,0\,0 \rangle$, respectively. The regularly spaced misfit dislocations are clearly visible in Fig. 4(b), which is a Fourier-filtered image of Fig. 4(a) using the $\bar{1}\,1\,0\,0_{ZnO}$ and $1\,\bar{1}\,0\,0_{ZnO}$ reflections and $1\,1\,\bar{2}\,0_{Al_2O_3}$ and $\bar{1}\,\bar{1}\,2\,0_{Al_2O_3}$ reflections. The positions of the misfit dislocations were marked by the arrows in Fig. 4(b). The in-plane translational period of ZnO along

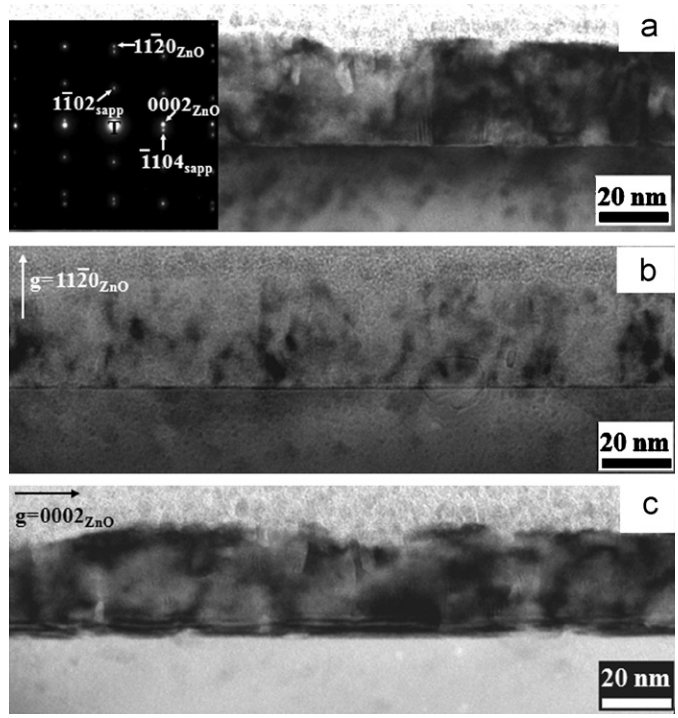

Fig. 3. Cross-sectional TEM micrographs of the 30 nm-thick ZnO film on Al_2O_3 $(1\,\bar{1}\,0\,2)$ substrate taken near the ZnO $[\bar{1}\,1\,0\,0]$ zone axis. (a) Zone axis BF micrograph, (b) $\mathbf{g} = 1\,1\,\bar{2}\,0_{ZnO}$ two-beam BF micrograph, and (c) $\mathbf{g} = 0\,0\,0\,2_{ZnO}$ two-beam BF micrograph. The diagonal contrast in the film and strain contrast of misfit dislocations at the interface are rarely observed.

the $[1\,\bar{1}\,0\,0]$ direction is $\sqrt{3}a_{ZnO} = 5.629$ Å, while the one for the Al_2O_3 $[\bar{1}\,\bar{1}\,2\,0]$ direction is $a_{Al_2O_3} = 4.758$ Å. From this, the lattice misfit (δ) along the ZnO $1\,\bar{1}\,0\,0$ direction is calculated to be 0.183. Therefore, the spacing (D) of the misfit dislocations is calculated to be 1.3 nm using the geometrically expected spacing of the misfit dislocations $D = |\mathbf{b}|/\delta$, where $|\mathbf{b}|$ is the magnitude of the Burgers vector component parallel to the interface, corresponds to 2.379 Å. This value is almost same with the observed spacing of misfit dislocations in Fig. 4(b). Unlike the HRTEM micrograph shown in Fig. 4(a), the HRTEM micrograph of Fig. 4(c), which was taken from the ZnO $\langle 1\,\bar{1}\,0\,0 \rangle$ zone axis, shows that ZnO planes are consecutively connected with sapphire planes at the interface. The translational period of ZnO along the $[0\,0\,0\,1]$ direction is $c_{ZnO} = 5.207$ Å, while the one for the Al_2O_3 $[\bar{1}\,1\,0\,1]$ direction is $\sqrt{3a^2_{Al_2O_3} + c^2_{Al_2O_3}} = 15.384$ Å. Therefore, the lattice misfit is as small as 1.54% along the ZnO $[0\,0\,0\,1]$ direction considering the domain matching epitaxy (DME) [17]. Because of this small value of lattice misfit along the ZnO $[0\,0\,0\,1]$ direction, the misfit dislocations are rarely observed from this zone axis. Fig. 4(d) is a Fourier-filtered image of Fig. 4(c) using the $0\,0\,0\,\bar{2}_{ZnO}$ and $0\,0\,0\,2_{ZnO}$ reflections and $1\bar{1}0\bar{4}_{Al_2O_3}$ and $\bar{1}104_{Al_2O_3}$ reflections, which shows the existence of one misfit dislocation at the interface. These results mean that the misfit and the strain relaxation by misfit dislocations are quite anisotropic in both perpendicular interfaces for the ZnO$(1\,1\,\bar{2}\,0)$/$Al_2O_3$$(1\,\bar{1}\,0\,2)$ heteroepitaxial system. The reason that only the ZnO $(0\,0\,0\,2)$ lattice planes are resolved in the HRTEM micrograph in Fig. 4(c) is due to the interplanar spacing of ZnO $(1\,1\,\bar{2}\,0)$ planes (1.625 Å) is below the point resolution of the used TEM instrument (the point resolution of the JEM 3010 microscope is 1.7 Å).

The samples with thicknesses of 90 and 180 nm were investigated by two-beam diffraction contrast imaging technique.

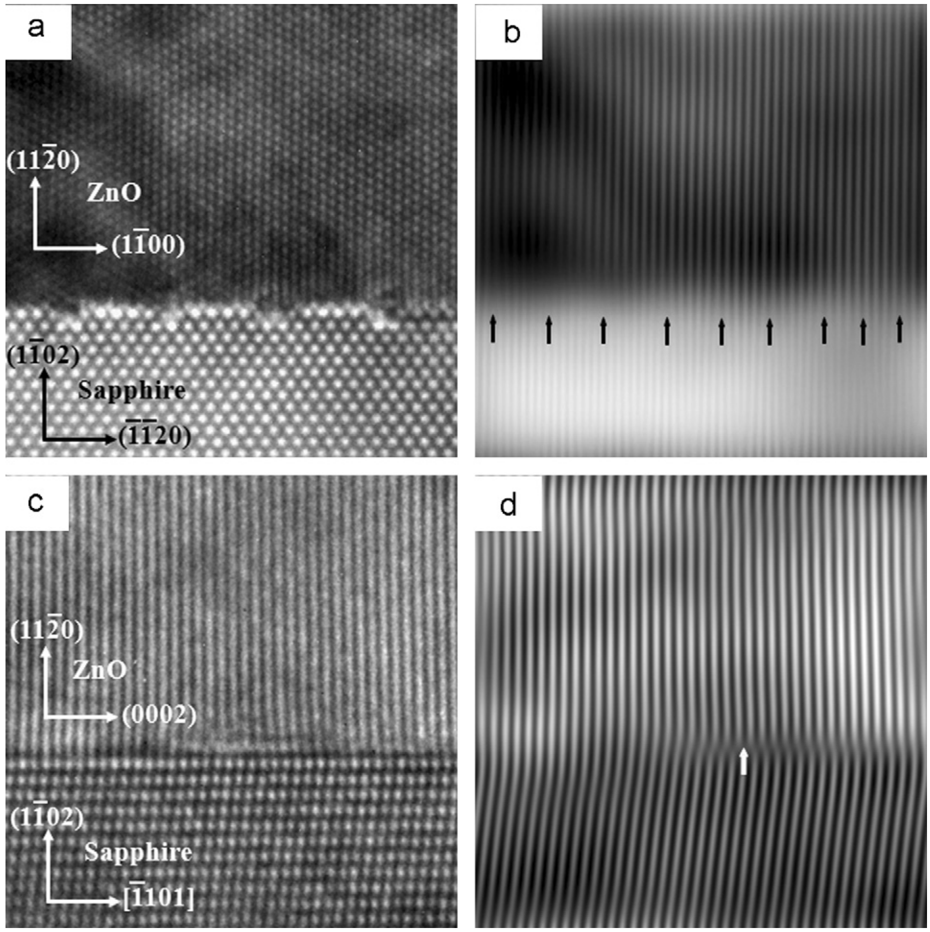

Fig. 4. HRTEM micrographs at the interfaces between ZnO (1 1 $\bar{2}$ 0) films and Al_2O_3 (1 $\bar{1}$ 0 2) substrates. (a) ZnO [0 0 0 1] zone axis HRTEM micrograph, (b) Fourier-filtered image corresponding to the image in (a), (c) ZnO [$\bar{1}$ 1 0 0] zone axis HRTEM micrograph, and (d) Fourier-filtered image corresponding to the image in (c). Misfit dislocations at the interfaces are marked by arrows.

Fig. 5(a) and (b) show, the cross-sectional TEM BF micrographs for the 90 and 180 nm-thick samples, respectively, obtained with the diffraction vector $\mathbf{g} = 1\,1\,\bar{2}\,0_{ZnO}$ under the ZnO $\langle 0\,0\,0\,1 \rangle$ zone axis. As shown in Fig. 5(a), very few diagonal contrasts were observed but a few curved threading dislocations were observed for the 90 nm-thick sample. However, in the case of 180 nm-thick sample, dominant threading dislocations were clearly observed and the diagonal contrast was difficult to be found as shown in Fig. 5(b). Therefore, the results of both Figs. 1 and 5 mean that the strain relaxation in the film is dominantly accommodated by the diagonal contrast in the thinner film but it is accommodated mainly by the threading dislocations in the thicker film.

Fig. 6 shows plan-view TEM BF micrographs with the diffraction vector $\mathbf{g} = 0\,0\,0\,2_{ZnO}$ and $1\,\bar{1}\,0\,0_{ZnO}$ for the same regions from 240 nm-thick ZnO film. By imaging with the different $\mathbf{g}$ vectors, the observed defects were very different. In Fig. 6(a) with $\mathbf{g} = 0\,0\,0\,2_{ZnO}$, the threading dislocations were observed without appearance of the stacking faults. Here, most of the dislocations are not straight line with a zigzag shapes, which appeared when the straight end-on dislocations were imaged in plan-view by titling. The irregular, curved shapes of threading dislocations appeared in Fig. 6(a) indicate that the dislocations were not thread straightly to the growth direction, i.e., the [1 1 $\bar{2}$ 0] direction.

Now, let's discuss the Burgers vector of threading dislocations in Fig. 6. For simplicity, if we only consider perfect dislocations in a hexagonal close-packed (hcp) crystal (we will discuss on the partial dislocations later), the Burgers vectors of dislocations in an hcp crystal should be one of $\frac{1}{3}\langle(1\,1\,\bar{2}\,0)\rangle$, $\frac{1}{3}(1\,1\,\bar{2}\,3)$, and $\langle 0\,0\,0\,1 \rangle$. In this case, the Burgers vector of the observed dislocations in Fig. 6(a) will be $\frac{1}{3}(1\,1\,\bar{2}\,3)$ or $\langle 0\,0\,0\,1 \rangle$ considering the $\mathbf{g}\cdot\mathbf{b}$ invisibility criteria since the image was obtained under the two-beam condition with $\mathbf{g} = 0\,0\,0\,2_{ZnO}$. In Fig. 6(b), we can see a few threading dislocations in addition to the major stacking faults. Burgers vector of these threading dislocations in Fig. 6(b) will be $\frac{1}{3}(1\,1\,\bar{2}\,3)$ or $\frac{1}{3}\langle 1\,1\,\bar{2}\,0 \rangle$ by the same consideration of the $\mathbf{g}\cdot\mathbf{b}$ invisibility criteria because those were imaged with $\mathbf{g} = 1\,\bar{1}\,0\,0_{ZnO}$. Since Fig. 6(a) and (b) are the micrographs from the same sample position, the dislocations with the Burgers vector of $\frac{1}{3}(1\,1\,\bar{2}\,3)$ should appear at the same sites in Fig. 6(a) and (b). However, most of the threading dislocations in Fig. 6(a) and (b) appeared at different sites, which means most of the threading dislocations in Fig. 6(a) have the Burgers vector of $\langle 0\,0\,0\,1 \rangle$, while the dislocations in Fig. 6(b) have the Burgers vector of $\frac{1}{3}\langle(1\,1\,\bar{2}\,0)\rangle$. In addition, we note that a higher density of threading dislocation were revealed in Fig. 6(a) than in Fig. 6(b), which means the major threading dislocation in the 240 nm-thick ZnO (1 1 $\bar{2}$ 0) film on Al_2O_3 (1 $\bar{1}$ 0 2) substrate in this study is the one with the Burgers vector of $\langle 0\,0\,0\,1 \rangle$. The dislocation densities in Fig. 6(a) and (b) were estimated to be $\sim 7.3 \times 10^{10}$ and $\sim 6.1 \times 10^{9}\,cm^{-2}$, which correspond to the dislocations with the Burgers vectors of $\langle 0\,0\,0\,1 \rangle$ and of $\frac{1}{3}\langle 1\,1\,\bar{2}\,0 \rangle$, respectively. Therefore, the total dislocation density was estimated to be $\sim 7.9 \times 10^{10}\,cm^{-2}$. Here, it should be noted that the threading dislocation along the growth direction with Burgers vector of $\langle 0\,0\,0\,1 \rangle$ is pure edge dislocation, where the Burgers vector is placed at in-plane. So, these

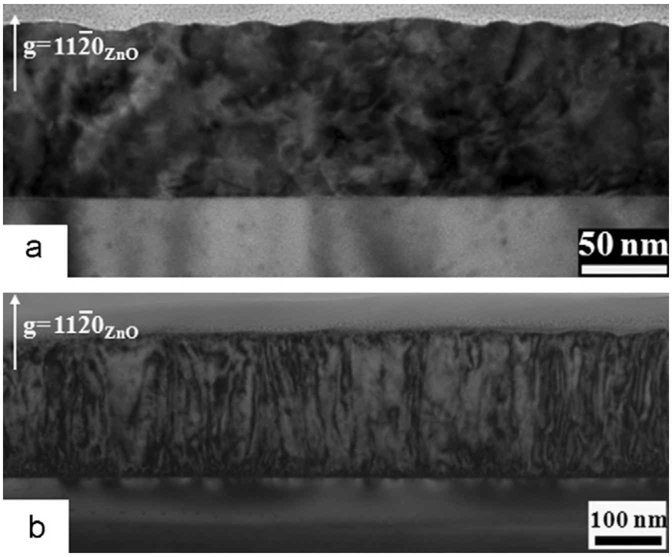

Fig. 5. Cross-sectional two-beam BF TEM micrographs of the 90 nm (a) and the 180 nm (b) thick-ZnO films taken near the ZnO [0 0 0 1] zone axis. The 90 nm-thick ZnO film showed a few diagonal contrasts with less threading dislocations, while the 180 nm-thick ZnO film showed very few diagonal contrasts with a great many threading dislocations as the major defect.

dislocations might contribute in the in-plane strain relaxation. However, the threading dislocation with the Burgers vector of $\frac{1}{3}\langle 1\,1\,\bar{2}\,0\rangle$ is pure screw dislocation, where the Burgers vector is placed at out-of-plane. The other possible dislocation with Burgers vector of $\frac{1}{3}\langle 0\,1\,\bar{1}\,0\rangle$ is partial dislocations with stacking fault of type-I_2 intrinsic [18,19]. Note that that the partial dislocations should accompany the stacking faults, which need a gain in energy formation compared with the perfect dislocations [20]. Also note that the type-I_2 intrinsic stacking fault has higher stacking fault energy than the type-I_1 intrinsic stacking fault [20]. This is believed as the reason that the most of stacking faults in our samples are the type-I_1 intrinsic stacking fault as discussed next.

Now, let us discuss the observed stacking faults in Fig. 6(b). In case of $\mathbf{g} = 1\,\bar{1}\,0\,0_{ZnO}$ two-beam condition, the stacking faults were exclusively observed as shown in Fig. 6(b), while not observed under $\mathbf{g} = 0\,0\,0\,2_{ZnO}$ in Fig. 6(a). The visibility of stacking fault can be determined according to the value of 'phase angle' $\alpha = 2\pi\mathbf{g}\cdot\mathbf{R}$, where $\mathbf{R}$ is the displacement vector of stacking fault. If $\alpha = 2\pi n$ (n is integers), the stacking fault will not be observed while if $\alpha \neq 2\pi n$, it will be observed at the TEM micrograph. In an hcp crystal, three kinds of stacking faults with displacement vectors of $\frac{1}{3}\langle 0\,1\,\bar{1}\,0\rangle$, $\frac{1}{2}\langle 0\,0\,0\,1\rangle$, and $\frac{1}{6}\langle 0\,2\,\bar{2}\,3\rangle$ are possible. For the stacking fault with a displacement vector of $\mathbf{R} = \frac{1}{6}\langle 0\,2\,\bar{2}\,3\rangle$, α is calculated to be 2π under the $\mathbf{g} = 0\,0\,0\,2_{ZnO}$ two-beam condition, while it is calculated to be $-(\frac{2}{3})\pi$ under the $\mathbf{g} = 1\,\bar{1}\,0\,0_{ZnO}$ two-beam condition. In case of the stacking fault with a displacement vector of $\mathbf{R} = \frac{1}{3}\langle 0\,1\,\bar{1}\,0\rangle$, α is calculated to be 0π under the $\mathbf{g} = 0\,0\,0\,2_{ZnO}$ two-beam condition, while it is calculated to be $-(\frac{2}{3})\pi$ under the $\mathbf{g} = 1\,\bar{1}\,0\,0_{ZnO}$ two-beam condition. Finally, in case of the stacking fault with a displacement vector of $\mathbf{R} = \frac{1}{2}\langle 0\,0\,0\,1\rangle$, α is calculated to be 2π under the $\mathbf{g} = 0\,0\,0\,2_{ZnO}$ two-beam condition, while it is calculated to be 0π under the $\mathbf{g} = 1\,\bar{1}\,0\,0_{ZnO}$ two-beam condition. Considering the results in Fig. 6(a) and (b) with different $\mathbf{g}$ vectors, the stacking faults observed in Fig. 6(b) are determined to be one of the stacking faults with the displacement vector of $\mathbf{R} = \frac{1}{6}\langle 0\,2\,\bar{2}\,3\rangle$ or $\mathbf{R} = \frac{1}{3}\langle 0\,1\,\bar{1}\,0\rangle$. Here, the stacking fault density was estimated to be $\sim 1.2\times 10^5\,\mathrm{cm}^{-1}$. Visibility and invisibility criteria for the perfect dislocations and stacking faults in an hcp crystal are summarized in the Table 1.

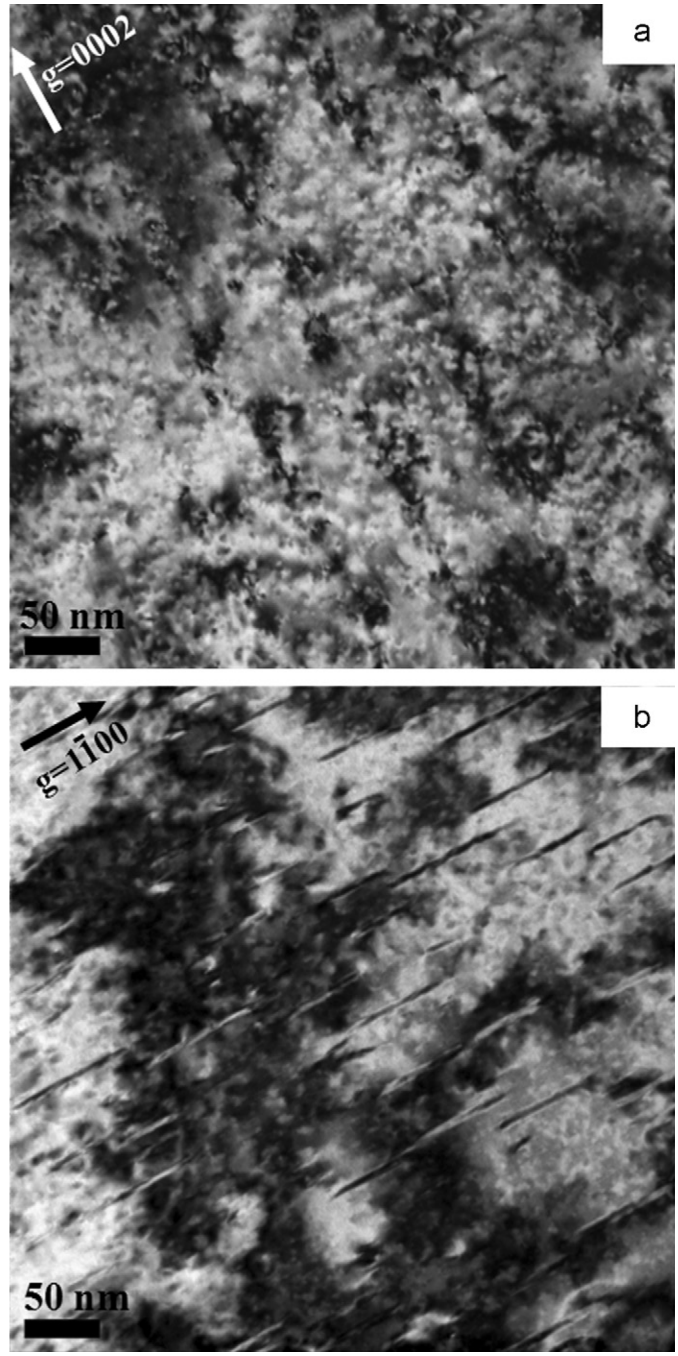

Fig. 6. Plan-view TEM micrographs of the 240 nm-thick ZnO film. (a) $\mathbf{g} = 0\,0\,0\,2_{ZnO}$ and (b) $\mathbf{g} = 1\,\bar{1}\,0\,0_{ZnO}$ two-beam BF micrographs. Perfect threading dislocations with a Burgers vector of $\langle 0\,0\,0\,1\rangle$ were dominantly observed in (a), while the stacking faults were mainly observed in (b).

In order to determine the exact type of stacking fault among the possible faults with $\mathbf{R} = \frac{1}{6}\langle 0\,2\,\bar{2}\,3\rangle$ or $\mathbf{R} = \frac{1}{3}\langle 0\,1\,\bar{1}\,0\rangle$, HRTEM study was performed. Fig. 7(a) shows a HRTEM micrograph for the stacking faults and the stacking sequence of the stacking fault was determined from the enlarged image in Fig. 7(b). The stacking sequence of ZnO (0 0 0 2) planes in the faulted region was determined to be AB'ABC'BCBC as shown in Fig. 7(b), which means the type of stacking fault is type-I_1 intrinsic stacking fault with a displacement vector of $\frac{1}{6}[0\,2\,\bar{2}\,3]$ [18,19]. The displacement vector was confirmed again by determining a Burgers vector of the partial dislocation bounding the stacking fault. As shown in Fig. 7(b), a Burgers loop is constructed at the end of stacking fault,

Table 1
Visibility and invisibility criteria for the perfect dislocations and stacking faults in an hcp crystal

	Burgers vectors of dislocations (**b**)			Displacement vectors of stacking faults (**R**)		
g	$\frac{1}{3}\langle 1\,1\,\bar{2}\,0\rangle$	$\langle 0\,0\,0\,1\rangle$	$\frac{1}{3}\langle 1\,1\,\bar{2}\,3\rangle$	$\frac{1}{6}[0\,2\,\bar{2}\,3]$	$\frac{1}{3}\langle 1\,0\,\bar{1}\,0\rangle$	$\frac{1}{2}\langle 0\,0\,0\,1\rangle$
0 0 0 2	Invisible	Visible	Visible	Invisible	Invisible	Invisible
$1\,\bar{1}\,0\,0$	Visible	Invisible	Visible	Visible	Visible	Invisible

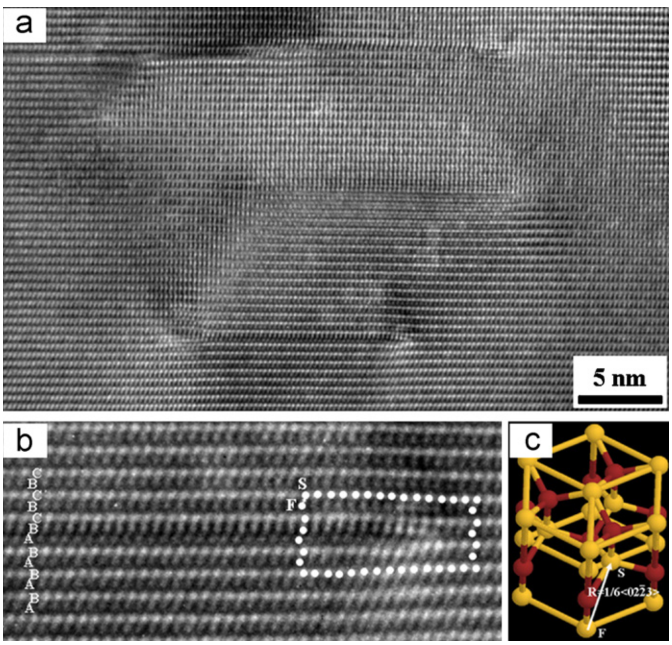

Fig. 7. (a) Plan-view HRTEM micrograph of the 240 nm-thick ZnO film. (b) Enlarged HRTEM micrograph of one of the stacking faults in (a). The stacking fault was determined to be a type-I_1 intrinsic stacking fault having the stacking sequence of (AB'ABC'BC) with bounding Frank partial dislocation with a Burgers vector of $\frac{1}{6}[0\,2\,\bar{2}\,3]$. (c) The magnitude and direction of displacement vector of $\frac{1}{6}[0\,2\,\bar{2}\,3]$ in a ZnO crystal are shown.

where the partial dislocation exists. The starting point (S) and the finish point (F) of the Burgers loop around the stacking fault did not coincide and the Burgers vector connecting the 'F' and the 'S' was determined to be $\frac{1}{6}[0\,2\,\bar{2}\,3]$, which is consistent with the displacement vector determined from the stacking sequence. The vector of $\frac{1}{6}[0\,2\,\bar{2}\,3]$ in an hcp crystal is shown in Fig. 7(c). Here, it should be noted that almost all of the stacking faults appeared in many other HRTEM micrographs showed the same features to the one in Fig. 7(b). Therefore, we have concluded that the major type of stacking faults in the ZnO film is the type-I_1 intrinsic stacking fault bounded by the Frank partial dislocation with the Burgers vector of $\frac{1}{6}[0\,2\,\bar{2}\,3]$. We note that the type-$I_1$ intrinsic stacking fault is the single fault involving one violation of the stacking rule, which means it is the stacking fault with the lowest stacking fault energy [20]. The stacking fault energy of type-I_1 intrinsic stacking fault is smaller than that of the type-I_2 intrinsic stacking fault bounded by the Shockley partial dislocation with the Burgers vector of $\frac{1}{3}[0\,1\,\bar{1}\,0]$ [20].

When discussing the threading dislocations of Fig. 6 in the previous, we considered the perfect dislocations only. Now, let us consider a possibility that the threading dislocations in Fig. 6 are being the partial dislocations not the perfect dislocations. The possible partial dislocations in an hcp crystal are the ones with the Burgers vector of $\frac{1}{6}[0\,2\,\bar{2}\,3]$, $\frac{1}{3}[0\,1\,\bar{1}\,0]$, and $\frac{1}{2}[0\,0\,0\,1]$, respectively. Since the faulted plane is (0 0 0 1), the partial dislocations shall run down to the image plane of Fig. 6, which means the partial dislocations shall be mostly the end-on dislocations. Also, since the partial dislocations are bounding the stacking faults, there should be a positional correlation between the threading dislocations in Fig. 6(a) and the stacking faults in Fig. 6(b) if the observed threading dislocations in Fig. 6(a) were partial dislocations. But, we could not find any positional correlation between the stacking faults in Fig. 6(b) and the threading dislocations in Fig. 6(a). Therefore, the most threading dislocations observed in Fig. 6(a) are not the partial dislocations bounding the stacking faults of Fig. 6(b). It means the threading dislocations in Fig. 6(a) are not the partial dislocations with the Burgers vector of $\frac{1}{6}[0\,2\,\bar{2}\,3]$. In addition, since Fig. 6(a) was taken with the $\mathbf{g} = 0\,0\,0\,2_{ZnO}$ two-beam condition, the partial dislocations with Burger vector of $\frac{1}{3}[0\,1\,\bar{1}\,0]$ should not be observed. Therefore, the threading dislocations in Fig. 6(a) are not the partial dislocations with the Burger vector of $\frac{1}{3}[0\,1\,\bar{1}\,0]$, too. Finally, in the case of partial dislocation with the Burgers vector of $\frac{1}{2}[0\,0\,0\,1]$, the stacking faults cannot be imaged under the two-beam conditions with $\mathbf{g} = 0\,0\,0\,2_{ZnO}$ or $1\,\bar{1}\,0\,0_{ZnO}$ considering the values of $\alpha = 2\pi\mathbf{g}\cdot\mathbf{R}$. At the same time, the partial dislocations with the Burgers vector of $\frac{1}{2}[0\,0\,0\,1]$ should be observed in Fig. 6(a) with $\mathbf{g} = 0\,0\,0\,2_{ZnO}$ and should not be observed in Fig. 6(b) with $\mathbf{g} = 1\,\bar{1}\,0\,0_{ZnO}$ two-beam condition. Therefore, it means that the threading dislocations in Fig. 6 can be a partial dislocation with the Burgers vector of $\frac{1}{2}[0\,0\,0\,1]$. However, the partial dislocation with the Burgers vector of $\frac{1}{2}[0\,0\,0\,1]$ bounds the extrinsic stacking fault with a stacking sequence of ABAB'C'ABAB. Since almost of the stacking faults observed in HRTEM study were the type-I_1 intrinsic stacking faults with a stacking sequence of AB'ABC'BC as mentioned before, we believe that the threading dislocations in Fig. 6 are not the partial dislocations with the Burgers vector of $\frac{1}{2}[0\,0\,0\,1]$. Here, it should be strongly noted that the extrinsic stacking fault is the triple fault containing three violations of the stacking rule and it can be formed by the insertion of c-layer but it cannot be formed by a single shear motion, which means that the formation of it during the film growth is highly difficult [20]. We also note that stacking fault energy of the extrinsic stacking fault is the highest among the stacking faults in an hcp crystal [20].

In Fig. 6(b), we can see a few threading dislocations in addition to the stacking faults. These dislocations are not the partial dislocation with the Burgers vector of $\frac{1}{2}[0\,0\,0\,1]$ because the image was taken under the two-beam condition with $\mathbf{g} = 1\,\bar{1}\,0\,0_{ZnO}$. Also these dislocations cannot be $\frac{1}{6}[0\,2\,\bar{2}\,3]$ nor $\frac{1}{3}[0\,1\,\bar{1}\,0]$ partial dislocations because such partial dislocations should reveal their stacking faults under the two-beam condition with $\mathbf{g} = 1\,\bar{1}\,0\,0_{ZnO}$ considering the values of $\alpha = 2\pi\mathbf{g}\cdot\mathbf{R}$. Therefore, we can conclude that the threading dislocations without the image of stacking faults in Fig. 6(b) are the perfect dislocations and the exclusive consideration of perfect dislocations except the partial dislocations in the previous discussion is reasonable.

Finally, let us discuss the threading dislocations investigated by cross-section TEM observations. Fig. 8(a) is a cross-sectional TEM BF micrograph of the 240 nm-thick ZnO film taken from the

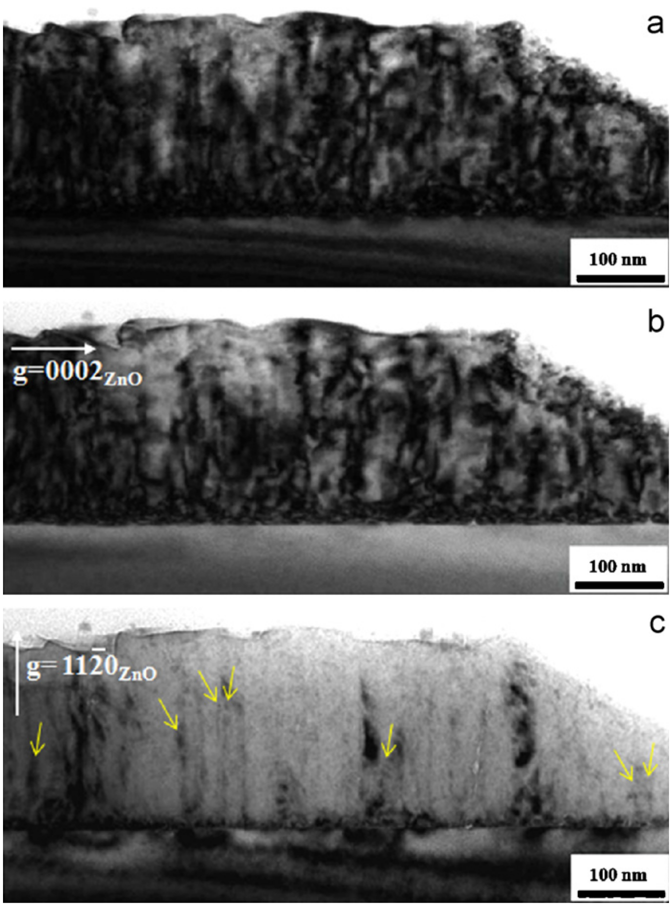

Fig. 8. Cross-sectional TEM micrographs of the 240 nm-thick ZnO film taken near the ZnO [$\bar{1}$ 1 0 0] zone axis. (a) Zone axis BF micrograph, (b) $\mathbf{g} = 0\,0\,0\,2_{ZnO}$, and (c) $\mathbf{g} = 1\,1\,\bar{2}\,0_{ZnO}$ two-beam BF micrographs. The marked threading dislocations by arrows and unmarked ones in (c) are the dislocations with a Burgers vector of $\frac{1}{3}\langle 1\,1\,\bar{2}\,3\rangle$ and $\frac{1}{3}\langle 1\,1\,\bar{2}\,0\rangle$, respectively. A many great number of dislocations were observed in (b). Almost of the threading dislocations in (b) have the Burgers vector of $\langle 0\,0\,0\,1\rangle$.

ZnO [$\bar{1}$ 1 0 0] zone axis. Fig. 8(b) and (c) shows cross-sectional TEM BF micrographs taken at the same region of Fig. 8(a) but imaged with the diffraction **g** vectors of $\mathbf{g} = 0\,0\,0\,2_{ZnO}$ and $\bar{1}\,1\,2\,0_{ZnO}$, respectively, under the two-beam conditions. Based on the $\mathbf{g} \cdot \mathbf{b}$ invisibility criteria, the threading dislocations observed in Fig. 8(b) should be the ones with the Burgers vector of $\langle 0\,0\,0\,1\rangle$ or $\frac{1}{3}\langle 1\,1\,\bar{2}\,3\rangle$, while the threading dislocations in Fig. 8(c) should have the Burgers vector of $\frac{1}{3}\langle 1\,1\,\bar{2}\,0\rangle$ or $\frac{1}{3}\langle 1\,1\,\bar{2}\,3\rangle$. Therefore, the dislocations appeared at the same positions of both Fig. 8(b) and (c) correspond to the threading dislocations with the Burgers vector of $\frac{1}{3}\langle 1\,1\,\bar{2}\,3\rangle$. These dislocations are marked by arrows in Fig. 8(c), therefore, the unmarked dislocations in Fig. 8(c) correspond to the dislocations with the Burgers vector of $\frac{1}{3}\langle 1\,1\,\bar{2}\,0\rangle$. On the other hand, a good many dislocations were observed in Fig. 8(b) with a much higher dislocation density. But, only a few dislocations of them were observed at the same positions in Fig. 8(c). This means almost of the threading dislocations in Fig. 8(b) should have the Burgers vector of $\langle 0\,0\,0\,1\rangle$. Therefore, we can reach to the same conclusion as the result from the plan-view observations in Fig. 6 that the major threading dislocations in the ZnO (1 1 $\bar{2}$ 0) film on Al_2O_3 (1 $\bar{1}$ 0 2) substrate have the Burgers vector of $\langle 0\,0\,0\,1\rangle$.

Another interesting feature of the threading dislocations from the cross-sectional views is that we can see very high density of threading dislocations at the interfacial regions of up to about 30 nm from the interface, where the dislocations were tangled each other as shown in Fig. 8(a) and (b). These dislocations were not imaged in Fig. 8(c), therefore, these dislocations should have the Burgers vector of $\langle 0\,0\,0\,1\rangle$. In addition, most of these dislocations did not thread to the upward direction but thread to the sideward direction. Finally, looking at Fig. 8(a) and (b), the number of threading dislocations is reduced as going to the upper region of film, which is believed to be resulted from the dislocation reactions at the interfacial region.

4. Conclusions

Microstructure and defects in nonpolar ZnO (1 1 $\bar{2}$ 0) films with different thicknesses were studied by TEM. The ZnO(1 1 $\bar{2}$ 0)/Al_2O_3(1 $\bar{1}$ 0 2) interface was observed to be atomically sharp and semicoherent. The lattice misfit along the ZnO [1 $\bar{1}$ 0 0] direction is calculated to be 0.183. The misfit dislocations were observed at the interface with regularly spaced configurations, which were well agreed with the equilibrium spacing of 1.3 nm. The lattice misfit along the ZnO [0 0 0 1] direction is as small as 1.54% based on the DME. Because of this small value of lattice misfit along the ZnO [0 0 0 1] direction, the misfit dislocations are rarely observed.

Although the lattice misfit was accommodated by regularly spaced misfit dislocations at the interface, the 'diagonal defect' along the ZnO [1 0 $\bar{1}$ 0] and [0 1 $\bar{1}$ 0] directions was mainly observed in the 30 nm-thick ZnO film instead of the threading dislocations. Considering the general fact that threading dislocations are concomitantly generated with misfit dislocations in the growth of lattice mismatched epitaxial thin films, very seldom appearance of threading dislocations in the thin ZnO films even with the regular formation of misfit dislocations is surprising. As increasing the film thickness, threading dislocations were being the major defects and the diagonal defects were seldom observed. However, the origin of diagonal defect was clarified in this study.

Very high density of tangled threading dislocations was observed in the 240 nm-thick sample at the interfacial regions of up to about 30 nm from the interface. Most of these dislocations did not thread to the upward direction but thread to the sideward direction. The density of threading dislocations was reduced as going to the upper region of film, which is believed to be resulted from the dislocation reactions at the interfacial region. Plan-view and cross-sectional observations using the two-beam diffraction contrast techniques revealed that almost all the threading dislocations have the Burgers vector of $\langle 0\,0\,0\,1\rangle$. The dislocation densities of the 240 nm-thick ZnO film were determined to be $\sim 7.3 \times 10^{10}$ and $\sim 6.1 \times 10^{9}\,cm^{-2}$, which correspond to the dislocations with the Burgers vectors of $\langle 0\,0\,0\,1\rangle$ and of $\frac{1}{3}\langle 1\,1\,\bar{2}\,0\rangle$, respectively, resulting in the total dislocation density of $\sim 7.9 \times 10^{10}\,cm^{-2}$.

In addition to the perfect threading dislocations, stacking faults on (0 0 0 1) planes were observed. From the two-beam diffraction contrast and HRTEM analyses, the stacking fault was determined to be the type-I_1 intrinsic stacking fault having a stacking sequence of (AB'ABC'BC) with bounding Frank partial dislocations, of which Burgers vector is $\frac{1}{6}$[0 2 $\bar{2}$ 3]. The stacking fault density of the 240 nm-thick ZnO film is determined to be $\sim 1.2 \times 10^{5}\,cm^{-1}$. The detailed microstructural characteristic of diagonal contrast was not clear at current status and further investigation is needed.

Acknowledgments

This work was supported by the Korea Science and Engineering Foundation (KOSEF) grant funded by the Korea government

(MOST) (No. R01-2007-000-20282-0) and also supported by Grant no. R11-2000-086-0000-0 (Center for Advanced Plasma Surface Technology) from the Center of Excellency Program of the KOSEF, MOST.

References

[1] D.M. Bagnall, Y.F. Chen, Z. Zhu, S. Koyama, M.Y. Shen, T. Goto, T. Yao, Appl. Phys. Lett. 70 (1997) 2230.
[2] T. Makino, K. Tamura, C.H. Chia, Y. Segawa, M. Kawasaki, A. Ohtomo, H. Koinuma, Appl. Phys. Lett. 81 (2002) 2355.
[3] C. Morhain, X. Tang, M. Teisserie-Doninelli, B. Lo, M. Laügt, J.-M. Chauveau, B. Vinter, O. Tottereau, P. Vennéguès, C. Deparis, G. Neu, Superlattices Microstructures 38 (2005) 455.
[4] T. Makino, A. Ohtomo, C.H. Chia, Y. Segawa, H. Koinuma, M. Kawasaki, Physica E 21 (2004) 671.
[5] T. Guillet, T. Bretagnon, T. Taliercio, P. Lefebvre, B. Gil, C. Morhain, X. Tang, Superlattices Microstructures 41 (2007) 352.
[6] B.P. Zhang, B.L. Liu, J.Z. Yu, Q.M. Wang, C.Y. Liu, Y.C. Liu, Y. Segawa, Appl. Phys. Lett. 90 (2007) 132113.
[7] J. Zúñiga-Pérez, V. Muñoz-Sanjosé, E. Palacios-Lidón, J. Colchero, Appl. Phys. Lett. 88 (2006) 261912.
[8] T. Moriyama, S. Fujita, Jpn. J. Appl. Phys. 44 (2005) 7919.
[9] S. Yamauchi, H. Handa, A. Nagayama, T. Hariu, Thin Solid Films 345 (1999) 12.
[10] S.K. Han, S.K. Hong, J.W. Lee, J.Y. Lee, J.H. Song, Y.S. Nam, S.K. Chang, T. Minegishi, T. Yao, J. Crystal Growth 309 (2007) 121.
[11] M.D. Craven, S.H. Lim, F. Wu, J.S. Speck, S.P. DenBaars, Appl. Phys. Lett. 81 (2002) 469.
[12] B.A. Haskell, F. Wu, S. Matsuda, M.D. Craven, P.T. Fini, S.P. DenBaars, J. Speck, S. Nakamura, Appl. Phys. Lett. 83 (2003) 1554.
[13] S.H. Lim, J. Vac. Sci. Technol. A 24 (2006) 264.
[14] S.H. Lim, D. Shindo, J. Appl. Phys. 88 (2000) 5107.
[15] D.N. Zakharov, Z. Liliental-Weber, B. Wagner, Z.J. Reitmeier, E.A. Preble, R.F. Davis, Phys. Rev. B 71 (2005) 235334.
[16] A.E. Romanov, W. Pompe, G.E. Beltz, J.S. Speck, Appl. Phys. Lett. 69 (1996) 3342.
[17] T. Zheleva, K. Jagannadham, J. Narayan, J. Appl. Phys. 75 (1994) 860.
[18] K. Dovidenko, S. Oktyabrsky, J. Narayan, J. Appl. Phys. 82 (1997) 4296.
[19] D. Gerthsen, D. Litvinov, Th. Gruber, C. Kirchner, A. Waag, Appl. Phys. Lett. 81 (2002) 3972.
[20] S. Amelinckx, in: F.R.N. Nabarro (Ed.), Dislocations in Solids, 2, North-Holland Publishing Company, Amsterdam, 1979, p. 88.